A Hovering Flapping-Wing Microrobot with Altitude Control and Passive Upright Stability

Z. E. Teoh, S. B. Fuller, P. Chirarattananon, N. O. Pérez-Arancibia, J. D. Greenberg and R. J. Wood

***Abstract*— The Harvard RoboBee is the first insect-scale flapping-wing robot weighing less than 100 mg that is able to lift its own weight. However, when flown without guide wires, this vehicle quickly tumbles after takeoff because of instability in its dynamics. Here, we show that by adding aerodynamic dampers, we can can alter the vehicle's dynamics to stabilize its upright orientation. We provide an analysis using wind tunnel experiments and a dynamic model. We demonstrate stable vertical takeoff, and using a marker-based external camera tracking system, hovering altitude control in an active feedback loop. These results provide a stable platform for both system dynamics characterization and unconstrained active maneuvers of the vehicle and represent the first known hovering demonstration of an insect-scale flapping-wing robot.**

I. Introduction

A number of challenges confront an engineer designing an autonomous insect-sized aerial vehicle. Components such as motors, bearings, and airfoils become inefficient as scale diminishes: surface effects increasingly dominate Newtonian forces [1] and viscous forces dominate lift-generating aerodynamic inertial forces [2]. Despite these challenges, various groups have reported success in building small scale aerial vehicles powered by rubber bands [3], small motors, propellors and rotary wings [4], [5], [6] citing their potential applications in search and rescue, artificial pollination, and reconnaissance. In our group we have made progress in solving these problems by taking inspiration from insects. We use muscle-like piezoelectric actuators to generate forces, flexures for pivot joints, and harness unsteady aerodynamic forces by flapping wings [7] because flapping-wing flight has been shown to be potentially more efficient than fixed-wing flight at insect-scale [8]. Our group has demonstrated constrained liftoff [7] and vertical position control [9] of the Harvard RoboBee, an insect-scale flapping-wing robot, using these techniques. Attaining unconstrained flight control, however, remains a challenge.

The fundamental innovation that enabled liftoff was an underactuated, passive mechanism that regulated the angle of attack of the wings [7]. This result stands in contrast to earlier efforts to actively control the exact angle of attack to reproduce the wing kinematics of flying insects. The design suffered from dynamic coupling and was not able to lift its own weight [10]. More recently, our group demonstrated that an underactuated mechanism could passively compensate for fabrication errors that resulted in bilateral asymmetry (such as by wing damage) using a differential-like mechanism [11]. These examples show that passive elements have an important role in simplifying the control of the RoboBee.

The authors are with the School of Engineering and Applied Sciences, Harvard University, Cambridge MA 02138 USA and the Wyss Institute for Biologically Inspired Engineering, Harvard University, Boston, MA 02115, USA (E-mail: zhiernteoh@seas.harvard.edu; minster@seas.harvard.edu; chirarat@fas.harvard.edu; nperez@seas.harvard.edu; jdgreenb@seas.harvard.edu; rjwood@eecs.harvard.edu)

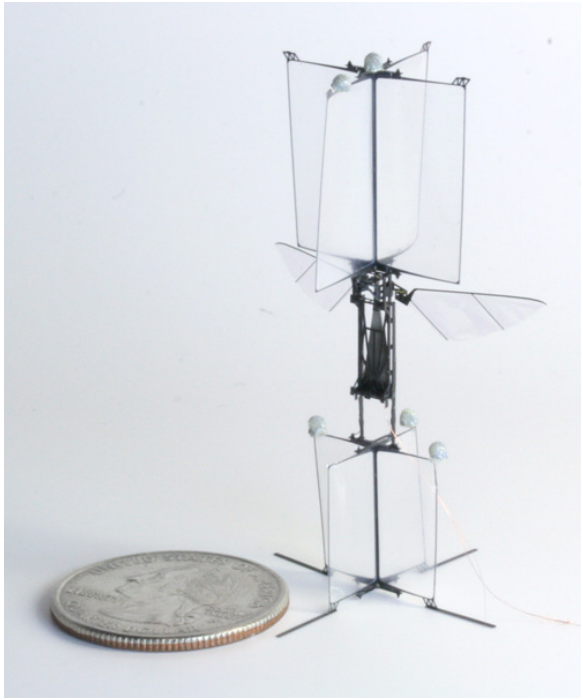

Fig. 1. Image of the RoboBee with 20 mm square top damper and 15 mm square bottom damper.

When scaling downward, in addition to increased surface effects and viscous forces, a further challenge emerges: the dynamics get faster as mass and moment of inertia decrease. To stabilize an unstable system such as the RoboBee, there is a maximum delay that can be tolerated in a feedback controller [12]. With diminishing scale, the time delays inherent in sensing and computation become increasingly problematic. Instead of active control, another approach is to use a passive, mechanical stabilizer, which incurs negligible time delay. In this work we show that lightweight passive air dampers, as shown in Figure 1, can stabilize the attitude of the RoboBee and simplify its design. This approach was inspired by demonstrations on larger flapping robots [13], but because the RoboBee is at a smaller scale, a more detailed analysis and characterization of the dampers' effect on the system's dynamics was required to find parameters that stabilized its flight. Though the passive dampers stabilize

upright orientation, they do not prevent active maneuvers driven by controlled changes in wing kinematics.

To measure the effect of flapping-wing aerodynamics on the dampers, we performed wind tunnel tests on the dampers and on a flapping-wing device to measure aerodynamic damping coefficients. From the wind tunnel measurements, we present a model and stability analysis that show how passive damping can stabilize the RoboBee's dynamics and use the model to choose proper damper size and positioning. We show that the behavior of the RoboBee is consistent with our simplified linear model which indicates that the stabilization of pitch angle θ (Figure 4) causes lateral motion due to a corresponding oscillation of the thrust vector during stabilization of θ.

Here, we define hovering to be sustained flight at a set altitude with small relative lateral drift rate. Using the dampers, the RoboBee was able to attain altitudes greater than 5 body length in vertical takeoff flights. Also, using a marker-based external camera tracking system, we performed closed loop altitude control for hovering flight which is the first demonstration of unconstrained active control of an insect-scale flapping-wing robot.

II. Wind Tunnel Tests

At the scale of the RoboBee, air drag on a vertically-oriented flat-plate damper is dominated by inertial forces which suggests that the lateral drag force F_D varies quadratically with relative air speed v according to

$$F_D = \frac{1}{2}\rho c_D(\alpha) A v^2 \quad (1)$$

where ρ is the air density, $c_D(\alpha)$ is the drag coefficient that varies with angle of attack α, and A the area of the damper.

Aerodynamic drag on the wings, however, is expected to vary proportionally with airspeed according to the following aerodynamic approximation: suppose the wing trajectory can be approximated as a upward-downward sawtooth function, neglecting the effects of wing rotation about the vertical axis and stroke reversal. Then with v, the free-stream airspeed and w, the velocity of the wings relative to the RoboBee, drag on the downstroke is $f_d = -\beta(v+w)^2$. On the upstroke, air drag reverses direction because the wings are moving much faster than the free-stream airspeed ($w \gg v$), and the drag force is $f_d = \beta(w-v)^2$. Since upstroke and downstroke take equal time, the stroke-averaged force is

$$\begin{aligned} \overline{f_d} &= \frac{1}{2}\beta(-v^2 - 2vw - w^2 + v^2 - 2vw + w^2) \\ &= -(2\beta w)v, \end{aligned} \quad (2)$$

showing how drag on the flapping wings is proportional to v for a constant w. The approximation can be extended to hold for rotating wings performing sinusoidal motion, assuming large w as is the case here.

To measure these forces, we carried out experiments to measure drag for wind speeds ranging from 0.00 ms^{-1} to 3.00 ms^{-1} in a wind tunnel. The wind speed was monitored and controlled with a PID controller, providing an accuracy

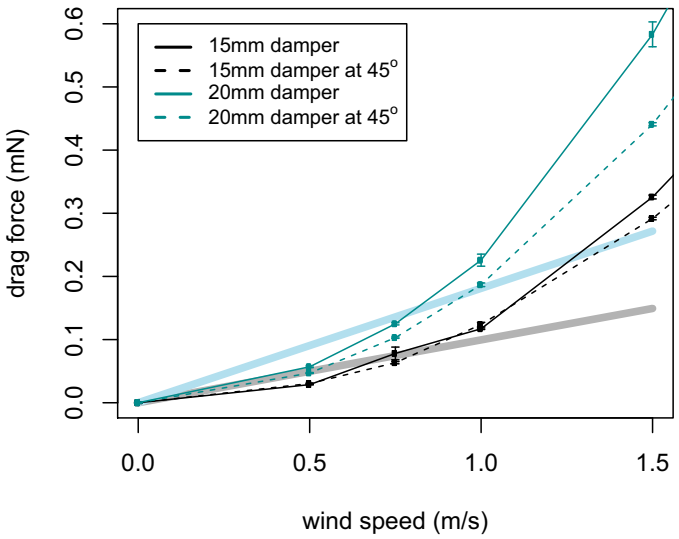

Fig. 2. Drag on the passive air dampers scales with wind velocity squared and damper area. If the damper is inclined 45° to the wind, drag diminishes only a small amount. At wind velocities up to 1.0 ms^{-1}, we approximate drag force as a linear function of the wind velocity. The linear approximation, calculated by linear regression up to 1.0 ms^{-1}, is shown by a thick line (error bars indicate one standard deviation).

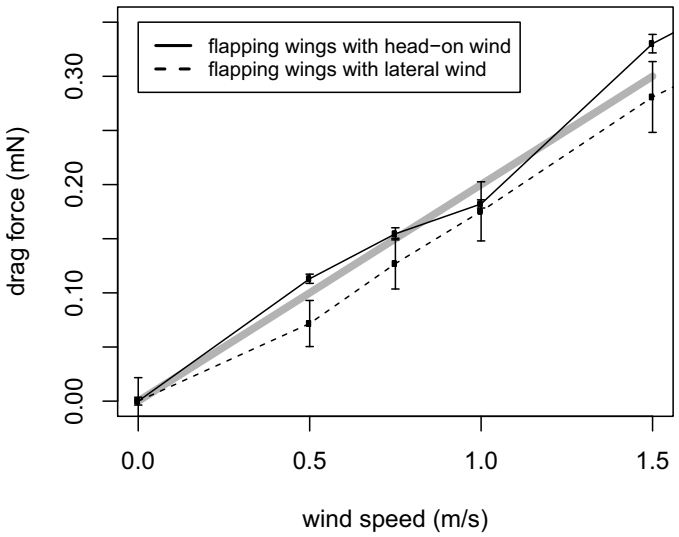

Fig. 3. Drag arising from flapping wings is approximately linear with airspeed and is also approximately equal for motion along either the x or y axis. The linear approximation is shown by a thick line.

of $\pm$0.01 ms^{-1}. The damper and/or the RoboBee was mounted at the end of a 30 cm moment arm attached to a precision six-axis force-torque sensor (*Nano17 Titanium*, ATI Industrial Automation, Apex NC USA) so that drag forces could be computed with high sensitivity from measured torque values (force sensitivity of $\pm$30 μN, sampled at 1000 Hz).

We considered two square damper sizes, 15 mm and 20 mm, each with two mounting orientations; perpendicular to the wind direction and at an angle of attack of 45°. The effect of drag on the mounting arm and/or the body of the robot was measured beforehand and subtracted out in the

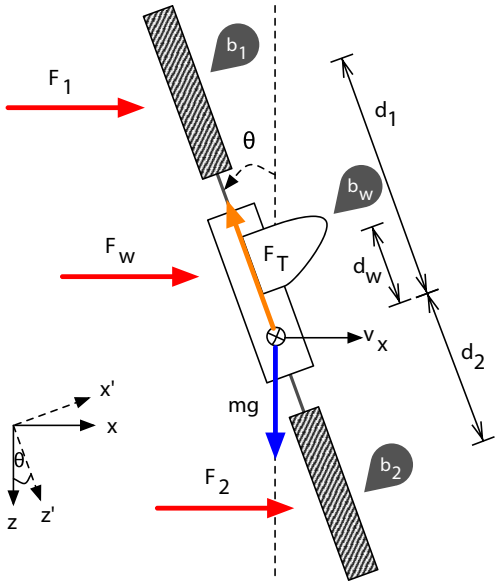

Fig. 4. Diagram of the lateral force and torque model for the RoboBee with passive dampers. Parameters include lateral velocity, v_x; pitch angle, θ; lift thrust force from flapping wings, F_t; lateral aerodynamic drag forces on dampers and wings, F_1, F_2, and F_w respectively; aerodynamic drag coefficients from dampers and wings, b and b_w respectively; distances from dampers to COM and distance from center of pressure of wings to COM, d_1, d_2 and d_w respectively.

appropriate plots. The plot of drag forces is displayed in Figure 2. As expected, drag force is consistent with (1), where lift and drag forces are quadratic functions of the air speed v. In Figure 3, drag on the wings varies linearly with airspeed as predicted by (2). If the RoboBee is rotated 90° about the inertial Z axis so that wind blows laterally across it rather than head-on, drag also approximates a nearly identical linear function. We do not have an aerodynamic model to explain this phenomenon, but remark that it simplifies analysis because both pitch and roll motions can be modeled with nearly the same dynamics.

Based on our wind tunnel measurements, we simplify the model in section III by approximating aerodynamic drag force as a linear function of the airspeed according to $f_d = -bv$. We estimated b by performing a least-squares linear regression on the force data of Figure 2 and Figure 3 for airspeed up to 1.0 ms^{-1}, giving damping coefficients for the 15 mm and 20 mm dampers and wings of $b_{15} = 1.0 \times 10^{-4}$ Nsm^{-1}, $b_{20} = 1.8 \times 10^{-4}$ Nsm^{-1}, and $b_w = 2.0 \times 10^{-4}$ Nsm^{-1}, respectively.

III. Model

To model a hovering state, we assume small θ and small vertical velocity, v_z. The primary task is to stabilize pitch angle θ with the lightest possible set of passive air dampers. A secondary consideration is to minimize drag to maintain maneuverability of the RoboBee. The dampers are oriented vertically at hover to produce aerodynamic drag during lateral motion. For stability, dampers are placed above and below the RoboBee's center of mass (COM) (Figure 4), as will be shown by our analysis.

As the RoboBee moves laterally, wind drag applies forces and corresponding torques about the COM as shown in Figure 4. Based on our wind tunnel experiments, we chose to approximate drag forces on both dampers and wings as linear with respect to the relative velocity of the surrounding air. Therefore, in our analysis, we model aerodynamic drag force according to $f_d = -bv$ (we assume that surrounding air does not move) where b is the aerodynamic damping coefficient that depends on damper and wing morphology and v is airspeed.

Equating the sum of lateral forces to acceleration (Figure 4),

$$\begin{aligned} m\dot{v}_x &= F_1 + F_2 + F_w + F_{t,l} \\ &= -b_1 (v_x - d_1 \omega c_\theta) - b_2 (v_x + d_2 \omega c_\theta) \\ &\quad -b_w (v_x - d_w \omega c_\theta) - F_t s_\theta, \end{aligned} \tag{3}$$

where c_θ and s_θ are shorthand for $\cos\theta$ and $\sin\theta$ and $F_{t,l}$ is the lateral component of the thrust force. Similarly equating torques to rotational acceleration,

$$\begin{aligned} J\dot{\omega} &= T_1 + T_w + T_2 \\ &= -d_1 F_1 + d_2 F_2 - d_w F_w \\ &= d_1 b_1 (v_x - d_1 \omega c_\theta) - d_2 b_2 (v_x + d_2 \omega c_\theta) \\ &\quad + d_w b_w (v_x - d_w \omega c_\theta) . \end{aligned} \tag{4}$$

Note that F_t does not appear here because its torque effect is zero as it intersects the COM.

Adding dampers is expected to change the moment of inertia of the vehicle, as well as its COM, so we must take into account this effect. We neglect the mass of the damper extension support structure which has a mass of 1 mg. We define r_w, r_1 and r_2 to be the distances from the RoboBee's center of mass (without dampers) to the distance of the stroke averaged center of pressure on the wings, to the center of masses of the top and bottom dampers, respectively. The new COM, after adding the mass of the dampers centered at these locations, moves to

$$r_{cm} = (-r_1 m_1 + r_2 m_2)/m, \tag{5}$$

where m_1 and m_2 are the masses of the top and bottom dampers and m is the mass of the entire vehicle, dampers included. Then we have

$$d_1 = r_1 + r_{cm} \tag{6}$$

$$d_2 = r_2 - r_{cm} \tag{7}$$

$$d_w = r_w + r_{cm} \tag{8}$$

and the total moment of inertia about the new COM of the RoboBee becomes

$$J = J_{bee} + m_{bee} r_{cm}^2 + J_1 + m_1 d_1^2 + J_2 + m_2 d_2^2 \tag{9}$$

where J_{bee} and m_{bee} correspond to moment of inertia and mass of the robotic bee by itself (without aerodynamic dampers).

The analysis for stability is simplified by linearizing the dynamics around $\theta = 0$ and by choosing identical top and bottom dampers ($b_1 = b_2 = b$) equidistant from the COM

TABLE I

PARAMETERS OF THE ROBOBEE SIMULATION.

Symbol	Name	case1	case 2	Units
b_1	top damper aerodynamic damping coefficient	1.8×10^{-4}	1.8×10^{-4}	Nsm^{-1}
b_2	bottom damper aerodynamic damping coefficient	1.8×10^{-4}	1.0×10^{-4}	Nsm^{-1}
b_w	flapping wings aerodynamic damping coefficient	2.0×10^{-4}	2.0×10^{-4}	Nsm^{-1}
d_1	top damper center to COM	18.2	26.9	mm
d_2	bottom damper center to COM	20.7	55.4	mm
d_w	wing center to COM	3.9	12.7	mm
J_{yy}	moment of inertia about COM	23.1	89.4	$\mathrm{g{\cdot}mm}^2$
m_1	mass of top damper(includes mass of 2 Vicon markers)	22	22	mg
m_2	mass of bottom damper(includes mass of 3 Vicon markers)	25	23	mg
m_{bee}	mass of the RoboBee (without dampers)	61	61	mg

($d_1 = d_2 = d$), enabling convenient term cancellations, giving

$$\dot{v}_x = \frac{1}{m}\left[\left(-2b - b_w\right) v_x - F_t\theta + b_w d_w \omega\right] \quad (10)$$

$$\dot{\theta} = \omega \quad (11)$$

$$\dot{\omega} = \frac{1}{J}\left[b_w d_w v_x + \left(-2bd^2 - b_w d_w^2\right)\omega\right]. \quad (12)$$

The state-transition matrix A in $\dot{x} = Ax$ for state vector $x = [v_x, \theta, \omega]^T$, assuming wing thrust balances weight $F_t = mg$, is

$$A = \begin{bmatrix} \frac{1}{m}\left(-2b - b_w\right) & -g & \frac{1}{m} b_w d_w \\ 0 & 0 & 1 \\ \frac{1}{J} b_w d_w & 0 & \frac{1}{J}\left(-2bd^2 - b_w d_w^2\right) \end{bmatrix} \quad (13)$$

We use the Routh-Hurwitz stability criterion to determine stability. This criterion depends on the characteristic equation $\det(A - \lambda I) = 0$, which is a polynomial of the form $a_3\lambda^3 + a_2\lambda^2 + a_1\lambda^1 + a_0 = 0$, and states that stability is assured if and only if all $a_k > 0$ and $a_2 a_1 > a_3 a_0$. All of the a_k terms are greater than 0 by inspection since mass and inertia must be positive and non-zero. Thus, the stability criterion reduces to

$$\frac{2b}{Jm^2}\left[\left(2b + b_w\right) d^2 + b_w d_w^2\right] \cdot \left[\left(2b + b_w\right) J + \left(b_w d_w^2 + 2bd^2\right) m\right] > b_w d_w g. \quad (14)$$

Assuming b_w is fixed by the flapping mechanism, if the factor b/Jm^2 is large enough, stability can be assured. Further, inside the left pair of brackets of (14), we can neglect $b_w d_w^2$ since $\left(2b + b_w\right) d^2 \gg b_w d_w^2$ because the dampers will be much farther from the COM than the wings ($d \gg d_w$) and based on wind tunnel measurements described in Section II, $b \sim b_w$, indicating that increasing d will also augment stability. Intuitively, stabilization of this simplified linear model can be assured by increasing rotational damping by either a large b, a large d, or a combination of both. Because m is dominated by the piezoelectric actuator of the flapping mechanism, it cannot be reduced by much and does not appear to be a route to optimization. The matter is slightly more complicated for reducing J, because as d increases, J increases to the square of d. One option to reduce the increase in J would be to increase b by making high aspect ratio dampers in the lateral direction. We leave optimization of these parameters to future work.

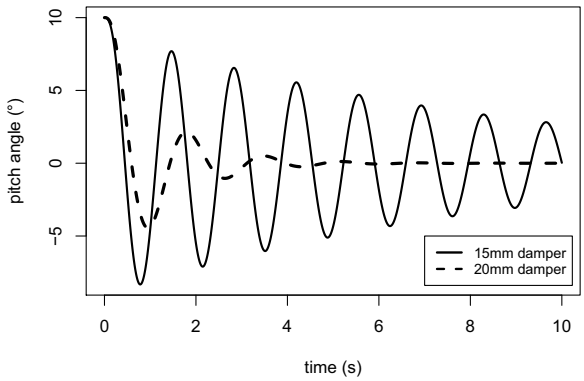

Fig. 5. Based on this simulation, the effect of decreasing the size of the bottom damper causes more oscillations during the recovery from an initial θ of 10°.

We used a free-body simulation to simulate forces and torques on the RoboBee. To augment the model, motion in the z axis was incorporated, wing and damper drag forces were assumed to act only perpendicular to damper surfaces, through their centers. Parameters used in the model are given in Table I (aerodynamic damping parameters were those found in Section II). We investigated the effect of the bottom damper on the RoboBee's dynamics by comparing the simulations of two cases. In case 1, the top and bottom damper are of the same size and at some $d_1$and d_2 (we chose the size and positions that satisfies the Routh-Hurwitz stability criterion). In case 2, we leave the top damper as in case 1 and decrease the size of the bottom sail. We set the stroke averaged thrust to the RoboBee's weight and start the simulations with an initial θ of 10°. Our simulations (Figure 5) indicate that a RoboBee having dampers of equal size will recover with less oscillations and in less time than one with a smaller bottom damper. To verify our simulations, we built a RoboBee that had features on its base to enable bottom dampers of different sizes and positions to be mounted.

IV. DESIGN AND FABRICATION

The RoboBee frame and transmission was based on the design that demonstrated constrained and controlled vertical flight [9].The design methodology of the RoboBee described in this paper was inspired by the design principles used

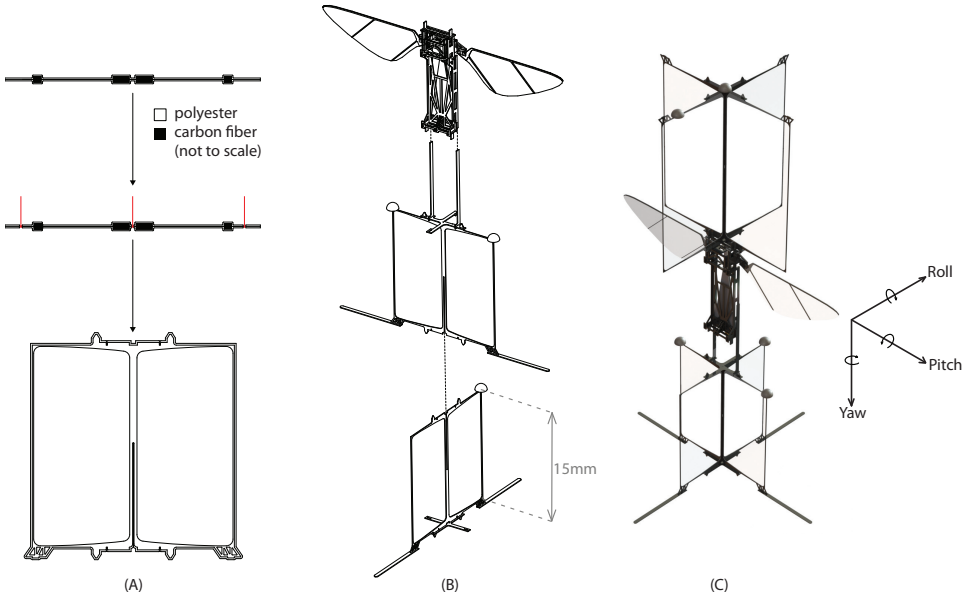

Fig. 6. (A) Damper fabrication consist of compressing a carbon fiber frame between two layers of polyester. The sandwich is cured under pressure and temperature to bond the polyester layers. After bonding, the damper is released by laser cutting the damper outline. (B) The bottom damper is assembled by sliding two dampers together to form a cross. The adjustment rail of the bottom damper is attached to the RoboBee along its side frame using a low temperature thermoplastic (Crystalbond™ 509, Electron Microscopy Sciences). (C) Solidworks rendering of the final assembly.

to create the monolithic bee of Sreetharan and pop up book MEMS techniques descibed by Whitney [14], [15]. It was designed to be assembled by employing a scaffold that combines the transmission and frame in a series of six folds. This technique decreases the number of discrete parts minimizing manual assembly while relying on alignment features within the scaffold to achieve alignment between the frame and transmission. This will be discussed in future work as we investigate ways to manufacture the RoboBee in a more automated and consistent manner.

The RoboBee has a top damper and a bottom damper. To make the dampers more robust to crashes during our experiments, the beams extending from the center of the damper were tapered to reduce the possibility of failure when the beams bend during crashes. Each damper consists of two intersecting surfaces that form a cross. The cross is fixed on both ends by caps that lock the dampers with respect to each other. Dampers were fabricated by sandwiching a laser-cut carbon fiber frame between two sheets of 1.5 μm polyester. Before sandwiching, the polyester is stress-relieved at its glass transition temperature, 150 °C for 1 minute, twice. The polyester film was melted and self-adhered in a heat press at 150 °C and 3.6 MPa for 15 min and allowed to cool under pressure in between 8 layers of teflon. The heat press enables the polyester membranes to merge, encapsulating the carbon fiber frame in the process. Once cooled, the outline is laser cut to release the damper from the sandwich.

To help us understand how the dampers affect the stability of our system, we fixed the size and position of the top damper but added an adjustment rail to the bottom damper so that its position could be varied to alter the system's dynamics. We fabricated two different bottom dampers: one 15 mm square and another 20 mm square.

V. Results

The prototype of the damper-stabilized RoboBee is shown in Figure 1. Because this RoboBee design does not have control authority over all degrees of freedom, particularly yaw rotation about its z' axis, in most flights the robot exhibited rotary motion in addition to lateral motion. To demonstrate upright stability during vertical flight, we drove the actuators with an amplitude of 230 V peak-to-peak at the resonant frequency of the RoboBee (105 Hz) causing it to accelerate upward. For this ascent, the smaller bottom damper with a shorter d_2 was sufficient to stabilize its vertical motion. Our current model does not capture the dynamics of the vertical ascent and we leave such modeling to future work. The power wire tether was made from three strands of 51 guage wire and its mass was negligible (less than 3 mg/m). We made sure that the power wire tether was not under tension during the ascent to eliminate the effects of a taut wire on the RoboBee. A composite image of a representative flight and a 3-dimensional (3D) plot of its trajectory is shown in Figure 7. Earlier attempts without the use of passive dampers were not successful because of the inherent instability of the RoboBee. This result is significant because it enables us to test free-flight without the use of vertical guide wires.

Next, we sought to demonstrate hover, which requires measurement and control of altitude during free flight. Based on our simulations, we chose to use the 20 mm damper on the top and bottom of the RoboBee. We attached five 1.5 mm spherical retroreflective markers (3 mg each, two on the top damper and three on the bottom damper) to the RoboBee so that its trajectory could be recorded with a

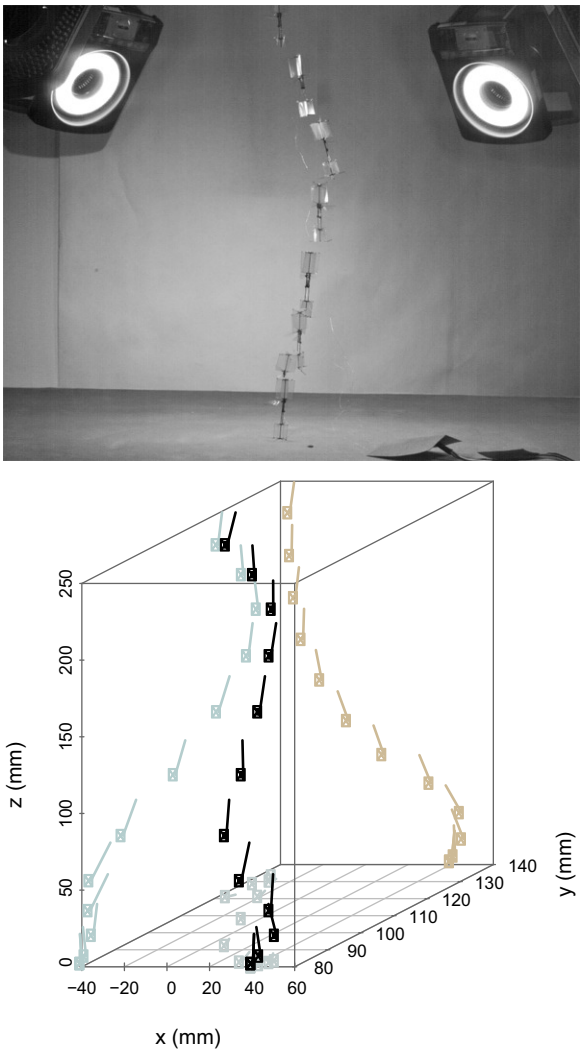

Fig. 7. Composite image from frames of a high speed video of a stable vertical takeoff by the damper-stabilized RoboBee with the corresponding 3D plot of its trajectory. Shutter speed was 1/500 s and frame interval is 0.1 s (top). A 3D plot of its trajectory (black) shown with its projections on the xy (grey), xz (beige) and yz (blue) plane (bottom). Each point in the 3D plot is 50 ms apart.

four-camera visual tracking system at 500 Hz (Vicon T040-series, Buckinghamshire, UK) with a 25-40 ms latency (our controller was able to perform its task with a 25 ms delay in simulation). Because the underactuated RoboBee does not have control over yaw or roll, we sought to stabilize to a desired altitude during a short time window before the bee drifted too far and exited the tracking volume (2.7×10^{-2} m^3), limiting the time period of the trials.

An XPC-target realtime PC (MathWorks, Natick, MA) received this pose information over serial port and computed voltage feedback commands at 10 KHz using a proportional-derivative (PD) controller. We regulated the altitude by modulating the amplitude of the voltage signal to the piezoelectric actuator using a P gain of $K_p = 900$ Vm^{-1} and a D gain of $K_d = 210$ Vsm^{-1} based on simulations of a simple model of the RoboBee's vertical dynamics consisting of its mass and air drag. These voltage amplitude commands were added to a nominal 216 V baseline feedforward signal that was the minimum amplitude necessary to achieve takeoff (though the voltage input is high, the current draw is less than 1 mA on average [16]). The derivative term was added to damp the vertical dynamics and add phase lead, based on wind tunnel drag data indicating that vertical aerodynamic drag has a damping factor of approximately 1.0×10^{-4} Nsm^{-1}. To minimize damage to the actuator and transmission of the bee, we limited the peak-to-peak voltage amplitudes to an interval that ranged from 200 to 256 V. As seen in Figure 8, the RoboBee has lateral drift which is caused by an inherent torque bias due to inevitable assembly asymmetry. Our linearized model predicts that there will be non-zero equilibrium θ in the presence of an inherent torque bias which tilts the thrust vector causing lateral drift. The lateral drift, however, does not play a role in the stability criterion in (14). This controller was able to stabilize the RoboBee's altitude with small error as shown in Figure 8, and could regulate altitude at a number of different altitude setpoints (75 mm, 100 mm, and 125 mm) as shown in Figure 9.

VI. Conclusions

We showed in this work that it is possible to stabilize vertical flight of a flapping-wing insect-scale robot and attain hover using passive aerodynamic dampers. Using a marker-based external camera tracking system, we were able to use active control to constrain the altitude of the RoboBee close to a desired setpoint for a second or two until it drifted out of the tracking volume. One important factor was an understanding of the dynamics of the aerodynamic dampers at hover, as well as an improved fabrication process for building the RoboBee that minimized unintended yaw torque enabling the dampers to stabilize its dynamics. This work provides a significant stepping stone for further flight control experiments by demonstrating a simple-to-build passively stable platform upon which system dynamics characterization and active maneuvers may be performed. With control over the RoboBee's yaw (z' axis) and roll (x' axis) torque ([17], [18]), arbitrary maneuvers could be performed, prolonging hovering flight indefinitely or enabling programmed trajectories.

For certain environments, such as outdoors where wind is prevalent, wind gusts may exert forces too great for a damper-equipped active flying robot to recover from, and so a more active controller may be necessary to eliminate the use of these dampers. We draw a parallel to flapping-wing insects, which eschew large wind-based dampers for this reason, and likely instead achieve stability by measuring their rotation rates, such as by their halteres [19], and performing a functionally equivalent damping action through changes in wing kinematics.

VII. Acknowledgements

This work was partially supported by the National Science Foundation (award numbers CCF-0926148 and CMMI-

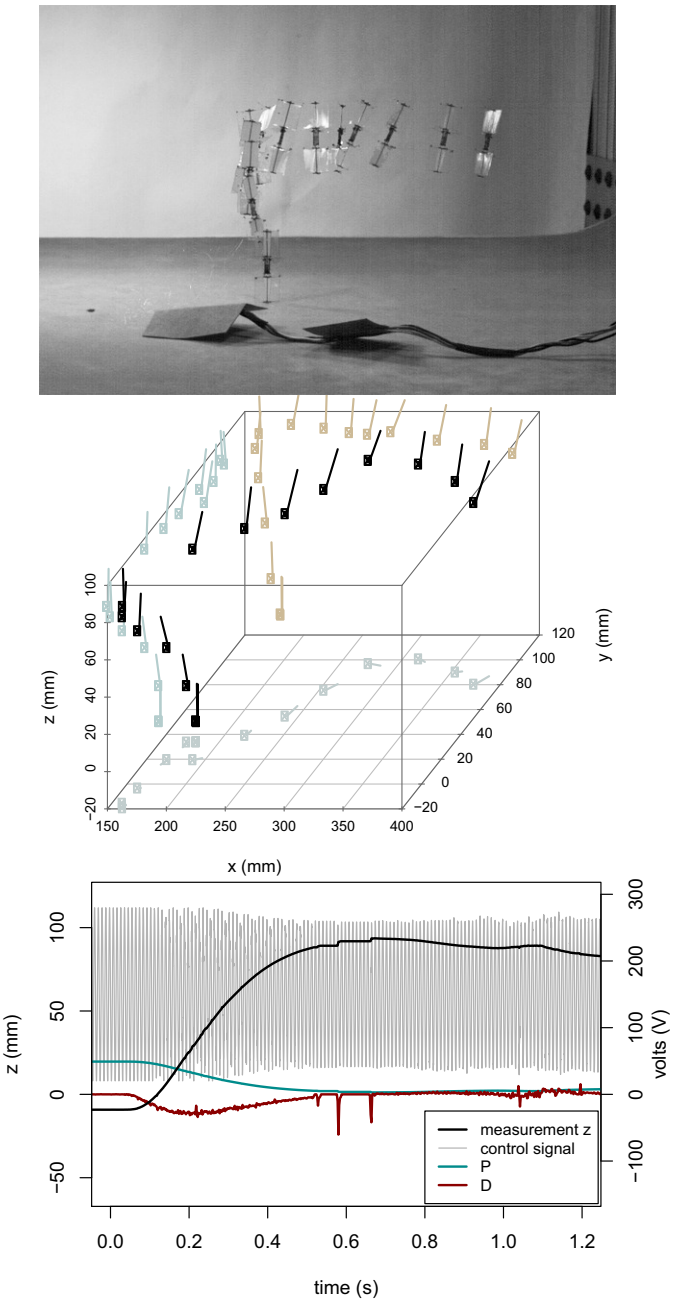

Fig. 8. Composite image from frames of a high speed video of altitude control of flapping microrobotic bee commanded to an altitude of 100 mm (top). Here the RoboBee accelerates vertically until reaching an altitude setpoint, then begins to drift laterally. A 3D plot of the RoboBee's trajectory (shown with its shadow) shows lateral drift in both the x and y axis which could be due to a combination of inherent torque bias and lateral motions during stabilization of θ. Each point in the 3D plot is 50 ms apart (middle). During the trial, we recorded the altitude measured by visual tracking (bottom, left axis), the P and D amplitude control commands, and piezoelectric actuator voltage during this trial run (bottom, right axis).

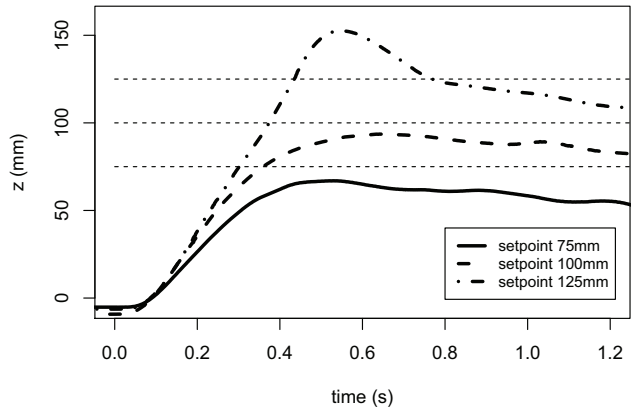

Fig. 9. RoboBee altitude during free-flight altitude control tests using a PD controller, recorded by visual tracking. The small error in the three cases is likely due to the steady-state error exhibited by PD controllers. The different altitudes demonstrate that the result is not due to the effect of the wire tether or an aerodynamic ground-effect.

0746638) and the Wyss Institute for Biologically Inspired Engineering. Any opinions, findings, and conclusions or recommendations expressed in this material are those of the authors and do not necessarily reflect the views of the National Science Foundation

REFERENCES

[1] W. S. N. Trimmer, "Microbots and micromechanical systems," *Sensors and Actuators*, vol. 19, pp. 267–287, 1989.

[2] M. H. Dickinson, F.-O. Lehmann, and S. P. Sane, "Wing rotation and the aerodynamic basis of insect flight," *Science*, vol. 204, pp. 1954–1960, 1999.

[3] H. Tanaka, K. Hoshino, K. Matsumoto, and I. Shimoyama, "Flight dynamics of a butterfly-type ornithopter," in *Intelligent Robots and Systems, 2005. (IROS 2005). 2005 IEEE/RSJ International Conference on*, aug. 2005, pp. 2706 – 2711.

[4] M. Keennon, K. Klingebiel, H. Won, and A. Andriukov, "Development of the nano hummingbird: A tailless flapping wing micro air vehicle," in *AIAA Aerospace Sciences Meeting*, 2012.

[5] I. Kroo and P. Kunz, "Development of the mesicopter: A miniature autonomous rotorcraft," in *American Helicopter Society (AHS) Vertical Lift Aircraft Design Conference, San Francisco, CA*, 2000.

[6] E. Ulrich, D. Pines, and J. Humbert, "From falling to flying: the path to powered flight of a robotic samara nano air vehicle," *Bioinspiration & Biomimetics*, vol. 5, p. 045009, 2010.

[7] R. J. Wood, "The first takeoff of a biologically inspired at-scale robotic insect," *IEEE Journal of Robotics and Automation*, vol. 24, no. 2, pp. 341–347, 2008.

[8] U. Pesavento and Z. Wang, "Flapping wing flight can save aerodynamic power compared to steady flight," *Physical review letters*, vol. 103, no. 11, p. 118102, 2009.

[9] N. Perez-Arancibia, Ma, K. C. Galloway, J. D. Greenberg, and R. J. Wood, "First controlled vertical flight of a biologically inspired microrobot." *Bioinspir Biomim*, vol. 6, no. 3, p. 036009, Sep 2011. [Online]. Available: http://dx.doi.org/10.1088/1748-3182/6/3/036009

[10] R. J. Wood, S. Avadhanula, M. Menon, and R. S. Fearing, "Microrobotics using composite materials: the micromechanical flying insect thorax," in *Proc. IEEE Int. Conf. Robotics and Automation ICRA '03*, vol. 2, 2003, pp. 1842–1849.

[11] P. S. Sreetharan and R. J. Wood, "Passive aerodynamic drag balancing in a flapping-wing robotic insect," *Journal of Mechanical Design*, vol. 132, no. 5, p. 051006, 2010. [Online]. Available: http://link.aip.org/link/?JMD/132/051006/1

[12] K. J. Astrom and R. M. Murray, *Feedback Systems: An Introduction for Scientists and Engineers*. 41 William Street, Princeton, NJ 08540: Princeton University Press, 2008.

[13] F. van Breugel, W. Regan, and H. Lipson, "From insects to machines," *IEEE Robotics & Automation Magazine*, vol. 15, no. 4, pp. 68–74, 2008.

[14] P. Sreetharan, J. Whitney, and R. Strauss M, and Wood, "Monolithic fabrication of millimeter-scale machines," *Journal of Micromechanics and Microengineering*, 2012.

[15] J. Whitney, P. Sreetharan, K. Ma, and R. Wood, "Pop-up book mems," *Journal of Micromechanics and Microengineering*, vol. 21, no. 11, pp. 115 021–115 027, 2011.

[16] M. Karpelson, J. Whitney, G. Wei, and R. Wood, "Design and fabrication of ultralight high-voltage power circuits for flapping-wing robotic insects," in *Applied Power Electronics Conference and Exposition (APEC), 2011 Twenty-Sixth Annual IEEE*. IEEE, 2011, pp. 2070–2077.

[17] B. Finio and R. Wood, "Open-loop roll, pitch and yaw torques for a robotic bee," in *Intelligent Robots and Systems (IROS), 2012 IEEE/RSJ International Conference on*. IEEE, 2012.

[18] K. Ma, S. Felton, and R. Wood, "Design, fabrication, and modeling of the split actuator microrobotic bee," in *Intelligent Robots and Systems (IROS), 2012 IEEE/RSJ International Conference on*. IEEE, 2012.

[19] M. Dickinson, "Haltere–mediated equilibrium reflexes of the fruit fly, drosophila melanogaster," *Philosophical Transactions of the Royal Society of London. Series B: Biological Sciences*, vol. 354, no. 1385, pp. 903–916, 1999.